Constitutive modelling of instabilities and strengths of an unsaturated tailings

Yanzhi Wang[1], *Thanh* Vo[2], and *Adrian* Russell[1*]

[1]Centre for Infrastructure Engineering and Safety, School of Civil and Environmental Engineering, UNSW Sydney, NSW, Australia
[2]School of Engineering, The University of Warwick, Coventry, UK.

Abstract. Instabilities mostly happen in fully saturated and loose non-cohesive geomaterials like sands or silts or tailings, but it is also possible in unsaturated geomaterials. When unsaturated they can experience a reduction in effective stress and strain soften during water (and air) undrained loading, attaining a very low residual strength. This study focuses on modelling the conditions required to cause instability in unsaturated silty tailings, giving particular consideration to the presence of air and the way it alters the ability for volume change when it remains trapped inside the tailings. A gold tailings is used to calibrate the UNSW bounding surface plasticity model. The effect of air, including the volumetric change caused by air compression, the alteration of air pressure, the contribution of suction to the effective stress, and suction hardening, are explored. Collapse lines (sometimes referred to as instability lines or flow liquefaction lines which represent boundaries between stable and potentially unstable stress states) in the $q - p'$ plane are explored. The undrained shear strength ratios and slopes of the collapse lines are compared to those of other tailings and sands when unsaturated.

1 Introduction

The leftover of mining and mineral extractions, tailings, are usually stored in Tailings Storage Facilities (TSFs) in a form of a solid-water-air mixture. Under certain loading conditions the tailings may reduce in strength significantly, and become unstable, causing the TSFs to fail. A very large volume of tailings may be released from the TSF and flow leading to catastrophic consequences. The shear strength of tailings in a TSF may reduce even when there is no apparent external disturbing load. Other factors, like creep or a rise in a phreatic surface, may be the cause. This kind of strength reduction under undrained loading is usually referred to as static liquefaction. When static liquefaction happens, the tailings may change from a solid-like material into a liquid-like material and spread for a long distance outside the TSF.

The stress ratio at the moment instability begins, η_{IL}, is an important parameter that controls the tailings structure collapse and the possible onset of liquefaction. Sladen *et al*. [1] was one of the first to highlight this, and found the stress ratio coincides with a collapse line. In very similar approaches others link the stress ratio to an instability line or flow liquefaction line, e.g. [2]. Each line coincides with the moment where the stress ratio reaches a peak and then reduces, sometimes significantly and rapidly. Considering Drucker's postulate, the instability point is the point where the second order work, d^2W, changes from a positive value to zero. For fully saturated conditions it is a simple task to quantify d^2W. For unsaturated conditions approximations have been made, specifically omitting the work done by the air-water interface, e.g. Buscarnera and his colleges [3] for the water undrained case and Wang *et al*. for the closed system case [4]. The instability points identified by these two approaches are extremely close to being identical.

Desaturation can enhance the stability of a natural soil or tailings, but there is no guarantee of safety from desaturation alone. There are many reported liquefactions of unsaturated tailings with sand or silt sized particles in either static or seismic conditions [5–11]. At a loose state a sample will reduce its volume when shearing causing the degree of saturation S_{r} to increase. The CSL and ICL in the $v - \ln p'$ plane will shift downward as a consequence. Another factor which reduces safety is the reduction of mean effective stress p' caused by the reduction of the effective suction, χs. This happens due to the corresponding reduction in shear strength ratio that accompanies a reduction of p', including when total stress is constant and suction decreases. According to the effective stress concept [12,13] :

$$p' = p + \chi s - u_{\mathrm{a}} \tag{1}$$

where p is the mean total stress, s is the suction, χ is the effective stress parameter and u_{a} is excess pore air pressure.

Silty tailings within the shallower portions in several TSFs, to depths of five to ten meters, have been observed to have an S_{r} ranging from 70% to 100% [14]. Sandy tailings tend to dry out more.

* Corresponding author: a.russell@unsw.edu.au

This research makes further contributions around instability, strength and collapse of an unsaturated silty tailings, giving particular consideration to the presence of air and the way it alters the ability for volume change when it remains trapped inside the tailings. The first part of the research presents an extension of UNSW's bounding surface plasticity model [15] and uses it to simulate a number of triaxial tests results in which static liquefaction is investigated. A variety of loading conditions, including (i) constant suction and (ii) closed system (constant mass) loading, are considered. The closed-system loading is particularly relevant to when fast deformations occur after the tailings becomes unstable. In the second part of the research the model is used to explore and simulate how a wider range of initial tailings states affect the propensity for instability and static liquefaction. A comparison is made between the constitutive model results and simulations from other reported sand and tailings samples.

2 Constitutive laws

The bounding surface plasticity model used in this research is that presented by Russell & Khalili [15]. A fast-loading event is assumed so that the air inside the sample is kept unvented to the atmosphere, i.e., a closed system with constant solid, water and air mass. Boyle's law is used to capture the air pressure and volume change in the closed system. Henry's law is ignored because of the fast-loading assumption. It has only a negligible influence.

The effective stress concept is used, expressed in Eq.1. The S_r and the variation of χ are functions of s and the air entry / expulsion suction:

$$S_\mathrm{r} = \begin{cases} 1 & \text{when } s \le s_\mathrm{e} \\ \left(\frac{s}{s_\mathrm{e}}\right)^{-\alpha} & \text{when } s \ge s_\mathrm{e} \end{cases} \tag{2}$$

and

$$\chi = \begin{cases} 1 & \text{for } \frac{s}{s_\mathrm{e}} \le 1 \\ \left(\frac{s}{s_\mathrm{e}}\right)^{-\Omega} & \text{for } \frac{s}{s_\mathrm{e}} \ge 1 \end{cases} \tag{3}$$

where s_e is the air entry suction ($s_\mathrm{ae} = C_1 e^{-D_\mathrm{s}}$) or air expulsion suction ($s_\mathrm{ex} = C_1 C_2 e^{-D_\mathrm{s}}$), C_1, C_2, α, D_s and Ω are material constants and e is the void ratio. The value used depends on whether the hydraulic state is drying or wetting.

Suction hardening is another important aspect influencing stability. The CSL is assumed to be a straight line which shifts depending on the suction ratio $SR = s/s_\mathrm{ex}$ according to:

$$v = \begin{cases} \Gamma(SR) - \lambda(SR)\ln(p') & \text{when } SR > 1 \\ \Gamma_\mathrm{sat} - \lambda_\mathrm{sat}\ln(p') & \text{when } SR \le 1 \end{cases} \tag{4}$$

where Γ is the intercept of the CSL with $p' = 1$ kPa and λ is the CSL slope. The saturated Γ and λ are constants and are denoted by a subscript $_\mathrm{sat}$. The unsaturated Γ and λ are functions of SR.

The loading surface, f, on which the current stress state $\boldsymbol{\sigma}'$ locates is surrounded by a bounding surface, F, linked through a mapping rule. Plastic deformation occurs when the current stress state lies inside or on the bounding surface. The unit normal vector controlling the direction of loading at $\boldsymbol{\sigma}'$ is $\mathbf{n} = [n_\mathrm{p} \quad n_\mathrm{q}]^\mathrm{T}$.

A non-associated flow rule is adopted meaning the plastic potential is different from the loading surface. The unit normal vector controlling the relative magnitudes of plastic strain increments is $\mathbf{m} = [m_\mathrm{p} \quad m_\mathrm{q}]^\mathrm{T}$.

The hardening modulus h comprises two additive parts, $h = h_\mathrm{b} + h_\mathrm{f}$. h_b relates to an image point $\overline{\boldsymbol{\sigma}}'$ on the bounding surface. h_f is an arbitrary modulus and is a function of the distance between $\boldsymbol{\sigma}'$ and $\overline{\boldsymbol{\sigma}}'$. $h_\mathrm{f} = 0$ when $\boldsymbol{\sigma}' = \overline{\boldsymbol{\sigma}}'$. The definitions adopted here are:

$$\begin{cases} h_\mathrm{b} = -\frac{\partial F}{\partial \overline{p}'_\mathrm{c}}\left(\frac{\partial \overline{p}'_\mathrm{c}}{\partial \varepsilon^\mathrm{p}_\mathrm{p}} + \frac{\partial \overline{p}'_\mathrm{c}}{\partial \gamma(SR)}\frac{\partial \gamma(SR)}{\partial SR}\frac{\dot{SR}}{\dot{\varepsilon}^\mathrm{p}_\mathrm{p}}\right)\frac{m_\mathrm{p}}{\left\|\frac{\partial F}{\partial \overline{\boldsymbol{\sigma}}}\right\|} \\ h_\mathrm{f} = k_\mathrm{m}\frac{\partial \overline{p}'_\mathrm{c}}{\partial \varepsilon^\mathrm{p}_\mathrm{p}}\frac{p'}{\overline{p}'_\mathrm{c}}\frac{(\overline{p}'_\mathrm{c} - p'_\mathrm{c})}{p'_\mathrm{c}} \end{cases} \tag{5}$$

where $\dot{}$ represent an incremental form, $k_\mathrm{m} = 0.1 + 0.025e^{-16\psi}$ is a component of h_f and may be defined in terms of the state parameter ψ [16] or some other measure of the state. $\gamma(SR)$ relates $\overline{p}'_\mathrm{c}$ on the unsaturated CSL to $\overline{p}'_{\mathrm{c}0}$, where $\overline{p}'_{\mathrm{c}0}$ is a corresponding parameter on the saturated CSL. $\gamma(SR)$ is defined after [17].

The volume and pressure of the air and water phases are described by combining [18] and Boyle's law:

$$\begin{cases} \dot{v_\mathrm{w}} = (S_\mathrm{r} + \frac{\partial S_\mathrm{r}}{\partial e})\dot{e} + \frac{\partial S_\mathrm{r}}{\partial s}\dot{s} \\ (u_\mathrm{a} + u_\mathrm{atm})\dot{v_\mathrm{a}} + \dot{u_\mathrm{a}}v_\mathrm{a} = 0 \end{cases} \tag{6}$$

where v_w and v_a are the specific volumes of the water and air, respectively, e is the void ratio and $u_\mathrm{atm} = 101.325$ kPa is the atmospheric air pressure.

3 Triaxial tests and model calibration

The model is now fitted to triaxial test results. The tailings, from a gold mine, is a sandy silt with a fines content of 59% and D_s = 2.618. It has a specific gravity of $G_\mathrm{s} = 2.78$, and a liquid limit and plastic limit of 18% and 16%, respectively [19,20]. Saturated triaxial tests were conducted to find the CSL [21]. The unsaturated triaxial test results considered here are for both: (i) constant s shearing and (ii) constant water and air mass (i.e. closed system) shearing.

3.1 Tests conducted

The constant s tests were conducted using a Bishop-Wesley triaxial testing system. Cylindrical samples 50 mm in diameter and 100 mm in height were used, formed by compacting three equal layers under a moisture content of 13%. The compacted e ranged from 0.719 to 0.771.

The samples were then moved in to the triaxial system. The pore water pressure, applied at the sample base, and cell pressure, were imposed by passing the laboratory's pressurised air through regulators via air-water interface cylinders. The pore air pressure, applied at the sample top, was imposed by passing the laboratory's pressurised air through a regulator. The axis translation technique [22] was then used to impose the target s, being ≈ 50 kPa or ≈ 150 kPa.

Closed-system tests were conducted using the same system. Samples were flushed to attain S_r values that ranged between 63% and 75%. The u_a was set to about 10kPa (above u_{atm}). The u_w was not measured as it was negative. Then, the valves connected to the air pressure and water pressure lines were closed and shearing commenced.

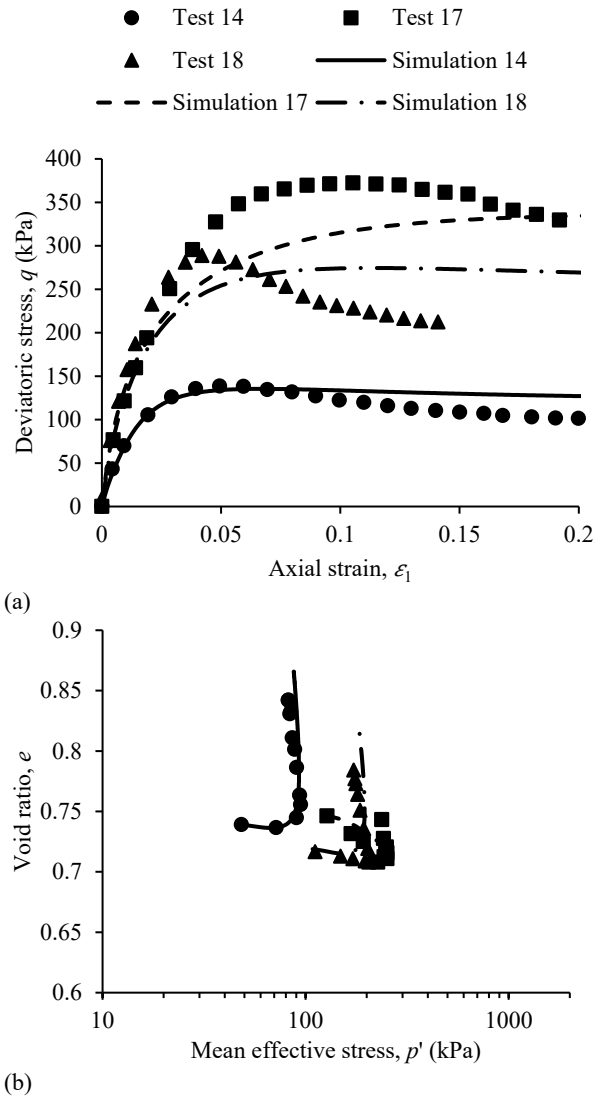

Fig. 1. Constant suction triaxial tests and simulation. The initial conditions are Test 14 ($s = 50.84$ kPa, $p_{n0} = 19.26$ kPa, $e_0 = 0.74$), Test 17 ($s = 51.82$ kPa, $p_{n0} = 98.11$ kPa, $e_0 = 0.75$) and Test 18 ($s = 150.18$ kPa, $p_{n0} = 48.04$ kPa, $e_0 = 0.72$)

3.2 Model calibration

The water retention curve (WRC) was determined through filter paper tests and pressure plate tests. The parameters are found to be $\alpha = 0.65$, $C_1 = 12$ kPa, $C_2 = 0.05$ [20]. $\Omega = 0.55$ is adopted for the χ relationship, meaning $\zeta = 0.15$.

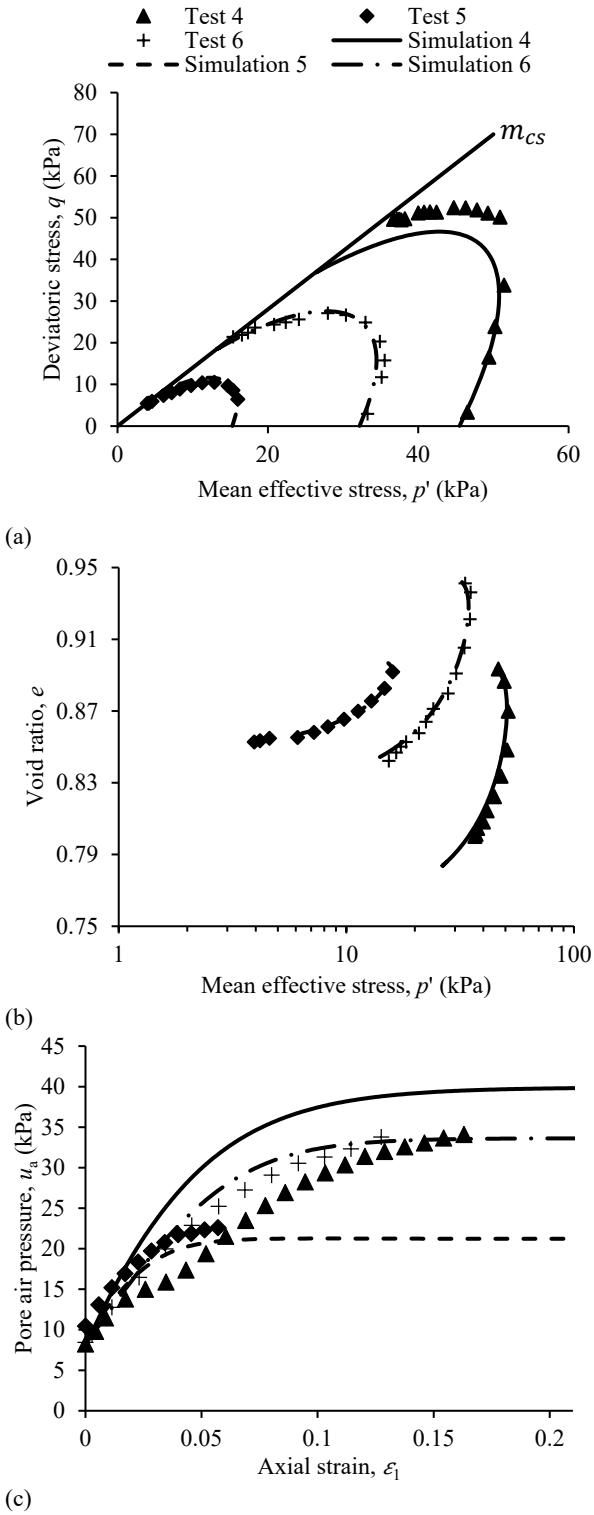

Fig. 2. Closed system shearing tests and model simulation. The initial conditions are Test 4 ($S_{r0} = 0.65$, $p_{n0} = 45.45$ kPa, $e_0 = 0.89$), Test 5 ($S_{r0} = 0.75$, $p_{n0} = 15.00$ kPa, $e_0 = 0.89$) and Test 6 ($S_{r0} = 0.63$, $p_{n0} = 32.30$ kPa, $e_0 = 0.94$)

The model is calibrated toward the tailings. The saturated CSL in the $v - \ln(p')$ plane [21] was fitted using $\lambda_{sat} = 0.036$ and $\Gamma_{sat} = 1.781$. The unsaturated Γ and λ in Eq. 4 are defined after [23]:

$$\begin{cases}\lambda(SR) = \lambda_{\text{sat}} + 4.5\left(SR^{0.004+\frac{0.015}{SR}} - 1\right) \\ \Gamma(SR) = \Gamma_{\text{sat}} + (\lambda - \lambda_{\text{sat}})\ln(2000)\end{cases} \quad (7)$$

The elastic parameter $\kappa = 0.009$ was found to be suitable.

Fig. 1 shows a selection of the constant suction test data and model simulations. Fig. 2 shows a selection of the closed system test data and model simulations. The performance of the model is better in closed system simulations than constant suction simulations. This is acceptable here since the main purpose of the model is to explore instability under high degrees of saturation when closed system conditions prevail.

4 Exploring the unsaturated instability

The calibrated model is used to explore instabilities of the gold tailings. The influences of total stress path, S_{r0}, $K_0 = \frac{q_0}{p_0'}$ and p_0' are considered. The subscript $_0$ represent the initial condition. A comparison is also made between the gold tailings in this research and other sand and tailings reported in the literature. The markers representing q_{peak} points in Figs. 3, 4, 5 and 6 also represent $d^2W \approx 0$ points – both conditions occur at (almost) exactly the same instances.

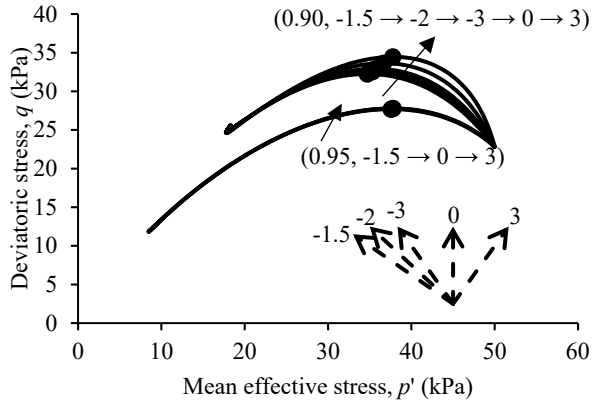

Fig. 3. Simulations of closed system shearing. $e_0 = 0.74$, $p_0' = 50$ kPa, $S_{\text{r0}} = 0.95$ and 0.9, total stress path $\delta q/\delta p$ ranges from -3 to 3, and $K_0 = 0.65$. The first number in each parentheses represents the S_{r0}. The numbers after the first comma represent $\delta q/\delta p$. Directions of arrows crossing the simulations show the change of $\delta q/\delta p$ and correspond to the → arrows in the parentheses. Arrows with dashed lines illustrate the directions of the total stress paths. In a clockwise direction they represent $\frac{\delta q}{\delta p} = -1.5, -2, -3, 0$ and 3. Markers represent q_{peak} points.

4.1 Total stress path influence

In a conventional triaxial compression test the total stress path is usually $\frac{\delta q}{\delta p} = 3$. It is quite different to this in a TSF. Fig. 3 shows that the total stress path influences the effective stress path, and the influences become increasingly pronounced as S_{r0} reduces. The total stress path therefore influences the absolute value of peak shear strength, but not η_{IL} significantly.

4.2 Other influencing factors

The influences of S_{r0}, K_0 and p_0' are also explored. Fig. 4 shows instability points from simulations. The slope η_{IL} is mainly affected by S_{r0} for a given ψ_0. The total stress path, K_0 and p_0' have less influence.

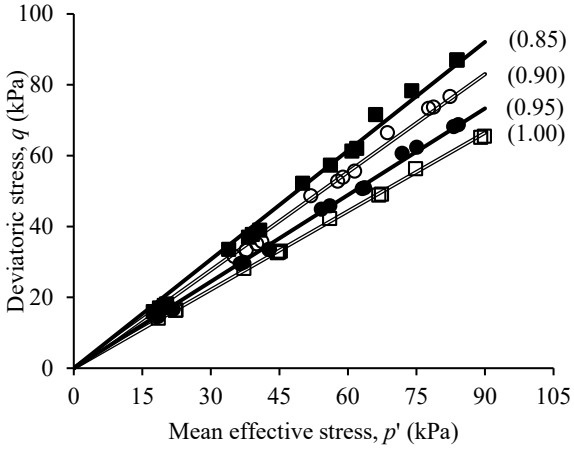

Fig. 4 Simulations of closed-system shearing, with markers representing q_{peak} ($d^2W \approx 0$). $S_{\text{r0}} = 0.85$, 0.9, 0.95 and 1.0, $K_0 = 0.65$ and 0.55, $\frac{\delta q}{\delta p} = 3$ and -1.5 and $p_0' =$25, 50, 75 and 100 kPa and $\psi_0 = 0.0598$ were used. Numbers in the parentheses represent S_{r0}

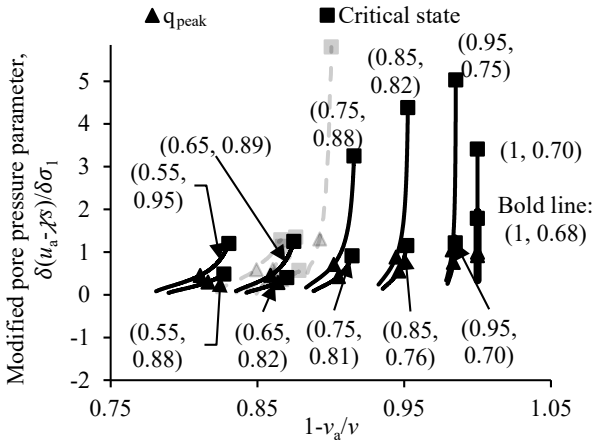

Fig. 5. Modified pore pressure parameter plotted against $(1 - v_{\text{a}}/v)$ for a series of simulations and closed system triaxial tests. The first number in the parentheses represent S_{r0} and the second number represent e_0. The simulations are plotted in black lines and the tests in grey lines to enhance visual clarity.

4.3 Combined effect of pore fluid pressure

The change of the combined pore fluid pressure, $(u_{\text{a}} - \chi s)$, relative to the change to the vertical total stress σ_1, is also explored with results shown in Fig. 5. The ratio between these changes is a type of pore pressure parameter that is a bit like $\bar{B}$ of Skempton. The combined pore fluid pressure is analogous to u_{w} for a fully saturated condition. For an unsaturated condition it captures the

combined effect of pore air and water pressures, and suction, on p'.

Other research [20] has shown that, under a fast loading condition, some geomaterials including this gold tailings behave quite differently when v_a/v is larger or smaller than a certain value of 0.15. When larger than 0.15 the geomaterials have behaviours that are similar to when saturated and drained – i.e. the solid skeleton is able to deform freely with little or no change to the pore pressures. When less than 0.15 there is too little air for the skeleton to compress or deform freely so a pseudo partially drained is more relevant.

Fig. 5 shows the incremental pore pressure parameter plotted against $(1 - v_a/v)$ for the closed system triaxial tests conducted and a series of simulations. This figure can be used to quickly determine the elevate a likely amount of combined pore pressure change for a variety of S_{r0} and e_0 values.

Table 1. Summary of data used in fig. 6.

1	[5]	Ottawa sand, microbially desaturated. Suction hardening is clearly shown in figures, but no fitted equations provided. Relative density is used to describe the sand state.
2	Triaxial extension, [5]	
3	Ottawa sand, [24]	$e_{CSL} = 0.92 - 0.0159\ln(p')$ for $p' < 250$ kPa; $e_{CSL} = 1.68 - 0.153\ln(p')$ for $p' < 250$ kPa according to [7]. No suction hardening information recorded
4	OZM 50 tailings, [6]	No suction hardening information recorded, $e_{CSL} = 0.908 - 0.0225\ln(p')$
5	Skarpa sand, [6]	No suction hardening information recorded, $e_{CSL} = 0.746 - 0.0635\log_{10}(p')$
6	Sample name unknown, [25]	Constant water content shear, no CSL information
7	Sand sample in Nanjing, China, [26]	Desaturated with biogas bubbles, no CSL information
8	Triaxial extension, [26]	
9	This research	Initially unsaturated

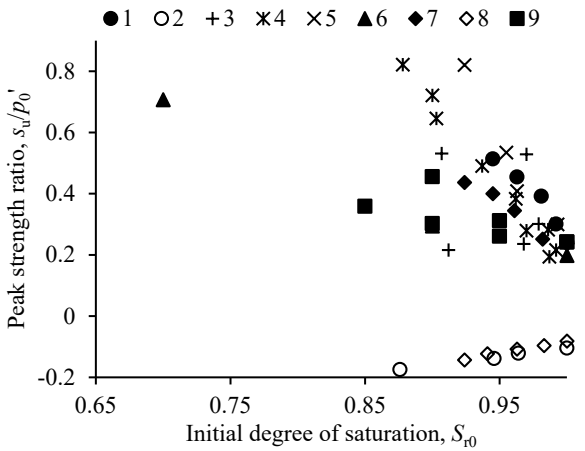

Fig. 6. s_u/p_0' plotted against S_{r0} for a variety of geomaterials.

4.4 Comparison with other materials

The undrained peak strength ratio, s_u/p_0', is often used for fully saturated conditions to characterise the strength, where $s_u = q_{peak}/2$. Here the concept is extended to unsaturated conditions. Although the closed system condition is different from a saturated undrained condition, they have similar peak shear strengths. The same notation, $s_u = q_{peak}/2$, is used.

Fig. 6 show s_u/p_0' values plotted against S_{r0} for a variety of geomaterials. Table 1 lists the data origins. A negative value of s_u represent triaxial extension tests.

5 Conclusion

The instability and strength of unsaturated tailings under a closed system loading condition are explored. The deformation towards failure under static loading is assumed to happen fast enough so the pore air does not have time to escape, given the tailings' low permeability. A bounding surface plasticity model is used to simulate the tailings' behaviour under the closed system condition. The effect of suction, both suction hardening and its contribution to the effective stress, is included in the model. Constant suction and closed system triaxial tests were used to calibrate the model. The calibrated model was then used to explore a variety of influencing factors, including the total stress path, initial degree of saturation, initial anisotropic consolidation and initial mean effective stress. The slope of the instability line, η_{IL}, was found to be mostly influenced by the degree of saturation for a given initial state parameter. Also, a combined pore fluid pressure parameter, when plotted against $(1 - v_a/v)$, depends on the initial degree of saturation and initial void ratio. Finally, the relationship between a peak shear strength ratio and initial degree of saturation, for this gold tailings and other sands and tailings reported in published papers, is similar.

This work forms part of TAILLIQ (Tailings Liquefaction), which is an Australian Research Council (ARC) Linkage Project (LP160101561) supported by financial and in-kind contributions from Anglo American, BHP, Freeport-McMoRan, Newmont, Rio Tinto and Teck. The TAILLIQ project is being carried out at The University of New South Wales, The University of South Australia, The University of Western Australia (lead organisation) and The University of Wollongong. We acknowledge the support and contributions of project personnel at each of the supporting organisations. The work also forms part of an ARC Future Fellowship (FT200100820) awarded to the corresponding author and that funding is gratefully acknowledged. Financial support from the China Scholarship Council is also gratefully acknowledged.

References

1. J. A. Sladen, R. D. D'Hollander, and J. Krahn, Can. Geotech. J. **22**, 564 (1985)
2. J. Chu and W. K. Leong, Geotechnique **52**, 751 (2002)

3. G. Buscarnera and C. di Prisco, International Journal for Numerical and Analytical Methods in Geomechanics **36**, 36 (2012)
4. Y. Wang, T. Vo, and A. R. Russell, Géotechnique (2023), https:://doi.org/10.1680/jgeot.22.00074
5. J. He and J. Chu, Journal of Geotechnical and Geoenvironmental Engineering **140**, 04014003 (2014)
6. W. Świdziński and M. Smyczyński, Applied Sciences **12**, 2076 (2022)
7. J. L. H. Grozic, The Behavior of Loose Gassy Sand and Its Susceptibility to Liquefaction, 1999
8. X. Lu, M. Huang, and J. Qian, in *Bifurcation and Degradation of Geomaterials with Engineering Applications*, edited by E. Papamichos, P. Papanastasiou, E. Pasternak, and A. Dyskin (Springer International Publishing, Cham, 2017), pp. 111–116
9. Z. Shi, S. Tong, and M. Huang, Engineering Geology **293**, 106296 (2021)
10. G. Bella and G. Musso, (2022)
11. R. Uzuoka, N. Sento, M. Kazama, and T. Unno, Soils and Foundations **45**, 149 (2005)
12. A. W. Bishop, Teknisk Ukeblad **39**, 859 (1959)
13. N. Khalili, F. Geiser, and G. E. Blight, International Journal of Geomechanics **4**, 115 (2004)
14. L. A. Oldecop, L. Garino, J. J. Muñoz, R. Rodríguez, and C. García, Unsaturated Soils, Taylor & Francis Group, London 1425 (2011)
15. A. R. Russell and N. Khalili, Int. J. Numer. Anal. Meth. Geomech. **30**, 181 (2006)
16. K. Been and M. G. Jefferies, Géotechnique **35**, 99 (1985)
17. B. Loret and N. Khalili, Mechanics of Materials **34**, 97 (2002)
18. H. Yang and A. R. Russell, Int. J. Numer. Anal. Meth. Geomech. **39**, 1975 (2015)
19. J. Ayala, A. Fourie, and D. Reid, Géotechnique Letters **10**, 492 (2020)
20. T. Vo, Y. Wang, and A. R. Russell, Géotechnique **72**, 274 (2022)
21. D. Reid, A. Fourie, J. L. Ayala, S. Dickinson, F. Ochoa-Cornejo, R. Fanni, J. Garfias, A. V. Da Fonseca, M. Ghafghazi, and C. Ovalle, Géotechnique **71**, 616 (2021)
22. J. W. Hilf, *An Investigation of Pore-Water Pressure in Compacted Cohesive Soils* (University of Colorado at Boulder, 1956)
23. A. R. Russell, T. Vo, J. Ayala, Y. Wang, D. Reid, and A. B. Fourie, Géotechnique 1 (2022)
24. J. L. Grozic, P. K. Robertson, and N. R. Morgenstern, Canadian Geotechnical Journal **37**, 843 (2000)
25. G. Buscarnera and R. Nova, International Journal for Numerical and Analytical Methods in Geomechanics **35**, 179 (2011)
26. E. Peng, Y. Sheng, X. Hu, D. Zhang, and Z. Hou, Journal of Environmental Management **295**, 113106 (2021)